Basic study of the relaxation volume of crystalline defects in bcc iron

M. El-Bakouri El-Haddaji[1], J.-P. Crocombette[2], A. Boulle[3], A. Chartier[4], A. Debelle[1]

[1]Université Paris-Saclay, CNRS/IN2P3, IJCLab, 91405 Orsay, France.

[2]Université Paris-Saclay, CEA, Service de Recherches de Métallurgie Physique (SRMP), 91191 Gif-sur-Yvette, France

[3]IRCER, CNRS UMR 7315, Centre Européen de la Céramique, 12 rue Atlantis, 87068 Limoges Cedex, France

[4]Université Paris-Saclay, CEA, Service de Corrosion et du Comportement des Matériaux dans leur Environnement (SCCME), 91191 Gif-sur-Yvette, France

Abstract

The relaxation volume (Ω^{rel}), here determined per extra-atom or vacant site, of common crystalline defects in bcc iron (Fe) was calculated from molecular dynamics simulation (MD) cells containing defects of varying size and/or density. To this end, we used both real and reciprocal space data: for the former, the change in the MD cell volume was calculated, while for the latter, we computed X-ray diffraction reciprocal space maps to evaluate the change in the lattice parameter. We show that <110> dumbbell self-interstitial atoms have the largest Ω^{rel}, ~1.5 atomic volume (~1.5 Ω_0). C15 clusters of size 12 and 48 atoms show Ω^{rel} of ~0.91 Ω_0 and ~0.98 Ω_0, respectively, and similar values are found for ½<111> and <100> interstitial dislocation loops, with Ω^{rel}~0.905 Ω_0 and Ω^{rel}~0.873 Ω_0, respectively. Single vacancies are characterized by a negative Ω^{rel}, ~-0.11 Ω_0. For cavities, Ω^{rel} rapidly increases to approach zero as the clusters grow. Using these values, we managed to predict (with an accuracy better than 2 %) the lattice strain in MD cells containing several types of defects, which indicates that the relaxation volumes can be summed up to estimate the microscopic (*i.e.,* lattice) volume change.

1. Introduction

Crystalline materials frequently lose part of their perfect atomic arrangement upon exposure to, e.g., temperature, stress or irradiation. The progressive loss of long-range order usually proceeds from the formation of crystalline defects, which are objects that locally introduce potentially large lattice distortions. These defects generally lead to a change in the physical properties of the materials, including thermal, electrical, electronic or mechanical properties. In all cases, defects affect the material behavior, the new response being wanted (as when semiconductors are doped or when steels are strengthened by shot peeing), or undesired (as for materials exposed to solar winds or radioactive decay for instance).

Defects in crystals are usually classified in two categories: (i) intrinsic defects, namely vacancy-type (V) and interstitial-type (I) defects and (ii) extrinsic defects, like impurities and dopants; we will not consider hereafter this latter type of defects. Among the first category, the smallest defects are the (0D) point defects, *i.e.,* the single vacancy and the self-interstitial atom (SIA) and their associated very small clusters. Characteristic energy properties of the intrinsic point defects, such as the migration and formation energies, can be adequately determined using electronic level simulations, as they are mainly determined by the very local defect neighborhood [1]. In contrast, these defects also generate long-range distortions of the lattice (see [2] and references therein) that can hardly be captured by electronic level calculations because of simulation-system size limitations. These perturbations lead to complex interactions with other defects that are subtle driving forces for the defects to migrate and cluster. 2D defects, such as dislocation loops, or 3D defects like cavities can then result from this defect clustering, and it is usually at this stage that the changes in the material properties are the most pronounced.

Another potential consequence of defect formation in crystalline materials is the development, when defects generate correlated atomic displacements (see [3] and references therein), of a lattice strain, *i.e.,* a change in the lattice parameter that leads to a microscopic volume change [4,5]. A macroscopic dimensional change can also take place, as it is for instance the case when large cavities form because interstitials agglomerate at dislocation loops, unbalancing the mobile V and SIA defect concentration [6,7]. These two volume changes can be accompanied by large-scale mechanical stresses [4], thereby compromising the material integrity. It is thus of utmost importance to predict them, which requires basic data such as, in particular for the lattice strain, the relaxation volume of the defects. This quantity can be described as the change in volume due to the relaxation of the crystal lattice around the defect site [4,5]. A dataset of relaxation volumes can be highly useful: it can be the principal ingredient in estimating the strains and stresses on a macroscopic scale [8], at least to some extent (see [9] for more details); it can also help exploiting experimental data, principally X-ray diffraction peak shifts related to elastic strain [10–12]. Relaxation volumes can be derived, for instance, from the elastic dipole tensor [4,13–18]. But in the present work, as explained hereafter, we present an alternative approach.

Iron-based materials are nowadays key materials for many structural components, and their presence in current and future (fission and fusion) nuclear power plants confirms this statement [19]. In such environments, materials are inherently subjected to extreme conditions, the most crucial one being the irradiation by energetic particles (neutrons, fission fragments, recoils…). Those particles are projectiles whose interactions with solid targets quasi-inevitably lead to defect creation. In the case of iron (Fe), an exhaustive literature exists regarding the defect panoply that can be found in this material submitted to irradiation (the reader can refer for instance to [20,21] and references therein). We shall here only recall the most important ones, which are listed considering a time evolution, *i.e.*, a progressive increase in irradiation dose. For interstitial-type defects, first, <110> dumbbell SIAs form, then C15 clusters, followed by ½<111> dislocation loops that are predominant at temperatures below ~670 K or <100> loops at higher temperatures [22,23]. Note that C15 clusters have been, so far, only predicted and not observed experimentally [24]. For vacancy-type defects, single vacancies can exist, as well as spherical clusters of these (so-called cavities) when the point defects can cluster; vacancy-type dislocation loops have been shown to be metastable [25].

Radiation-induced microstructural changes and associated physical property modifications are processes that intrinsically encompass orders of magnitudes in terms of time and space scales. A thorough understanding of these processes not only requires a broad range of experiments, but also a comprehensive multiscale modelling [26,27]. To feed the models step by step, one needs basic, atomic-scale data, the availability of which remains the cornerstone aspect of the current intense effort in the development of the multiscale modelling of materials. In the current paper, we precisely address this matter, *i.e.*, we provide basic defect characteristics. Indeed, we propose an *in silico* method that combines large-scale Molecular Dynamics (MD) simulations with computational diffraction for a dual, *i.e.*, in both real and reciprocal spaces, determination of the relaxation volume of the most important defects in iron, chosen as a test-case material. We performed a systematic, parametric study in which broad defect concentrations, as well as various defect configurations were investigated. Results not only provide quantitative data on the relaxation volumes, but they also show that this quantity can be summed up when several defects, of the same type or of different nature, are simultaneously considered.

2. Methodology

2.1. Generation of MD cells containing defects

Model molecular dynamics cells were created by generating in a controlled manner defects in perfect single-crystal-like bcc iron cells of 80x80x80 unit cells (u.c.) in dimension, *i.e.*, cubic cells containing 1 024 000 atoms and with a side length of 22.8 nm (except for cells with C15 clusters whose size was 90x90x90 unit cells – 1 458 000 atoms - and a side length of 25.7 nm). The lattice parameter of the pristine cells was a_0 = 0.28557 nm at 0 K, according to the M10 interatomic potential used here [28]. The suitability of this EAM potential regarding the reproduction of the elastic properties of different crystalline defects was validated by comparison with DFT data [28]. Defects of both interstitial and vacancy nature were created, but only one defect type was introduced, in a first time, in each cell (in a second time, cells with mixed defects were created, see sect. 4). For both Is and Vs, several defect structures were studied. The corresponding MD cell characteristics are given in sections 2.1.1 and 2.1.2. Note that those characteristics were chosen to cover the largest defect concentration and size ranges while taking into consideration the computational capabilities. Therefore, not all characteristics are consistent from one set of cells to another. Note also that, in order to limit the forces acting on the atoms constituting or surrounding a defect (particularly interstitial ones), and hence to facilitate the relaxation process (details of which can be found in section 2.1.3), we imposed a separation distance between the defects. This latter varied according to the defect type, nature, size and density, but was typically in the range of a few nm. To finish, it is important to mention that imposing a separation distance between the defects during the defect injection step does not imply that those defects do not interact during the relaxation step, particularly at high defect density (see for instance results for dumbbells in Fig. 5a).

2.1.1. Interstitial-type defects

For interstitial defects, three configurations were examined: <110> dumbbell SIAs, C15 clusters and dislocation loops (of both <100> and ½<111> types). As for these MD cells, Fe atoms were injected to form the defects, we will talk about *extra-atoms* in the cells, and their corresponding number N_{extra} and concentration C_{extra} are given in Table 1; also provided in Table 1 are the defect number (N_I), radius (R_I) and density (ρ_I).

Let us start with <110> dumbbell SIAs. Those defects were added into pristine MD cells with a concentration of up to 1.4 % (for these defects, N_I=N_{extra}). For this purpose, a two-step procedure was implement0ed. First, one cell was created, containing a few dumbbells in the form of two atoms oriented along the chosen <110> direction and separated by a reasonable distance (*viz.* 1/2 of the <110> diagonal of a unit cell, *i.e.,* 0.202 nm). This cell was then relaxed (see *sect. 2.1.3*), and the coordinates of the two atoms constituting each dumbbell was used to calculate the average characteristic separation distance

between both atoms. This characteristic distance, found to be 0.2156 nm, was used to facilitate the relaxation process of the cells containing a large dumbbell concentration for which this distance was chosen as the initial separation length. Note that a value of 0.1905 nm was found by DFT [29]. In a second step, a given number of atoms of the perfect crystal was randomly selected and replaced by <110>-type di-atomic dumbbells, each precise direction being randomly chosen among the 6 equivalent directions. The net number of SIAs after the generation of a <110> dumbbell SIA is hence 1 (2 added atoms – 1 removed atom per dumbbell). Fig. 1a shows a picture, generated with the OVITO software [30], of a relaxed cell with 0.02 % of <110> dumbbell SIAs.

The structure of C15 clusters is more complex than that of dumbbells. Their geometry corresponds to a Z16 Frank-Kasper polyhedron with (at least) 12 interstitial atoms and (at least) 10 vacancies in a bcc structure. Hence, atoms in a C15 cluster exhibit an icosahedral coordination. Cells with C15 clusters were generated with a net extra-atom concentration of up to 0.41 %. Two C15 cluster sizes were considered, 12 and 48 atoms (hereafter denoted as $C15_{12}$ and $C15_{48}$, respectively); note that the critical size of 51 atoms, where C15 clusters tend to transform into dislocation loops [31], was not exceeded. The generation of the cells containing those clusters was carried out by (i) randomly selecting the central C15 atom, then (ii) removing 10 (38) closest atoms and finally (iii) adding 12 (48) atoms with the previously explained polyhedron geometry, illustrated in [31], with a net number of 2 (10) SIAs in the $C15_{12}$ ($C15_{48}$) defects, respectively. Fig. 1b shows a relaxed cell containing $C15_{48}$ clusters; $C15_{12}$ and $C15_{48}$ cluster structures are illustrated in Fig. 1c.

Both <100> and ½<111> interstitial dislocation loops (referred to as L_{100} and L_{111}, respectively) were here studied, with a net extra-atom concentration reaching 1.5 % for some MD cells. For each orientation, three sets of defective cells were generated. The Babel code [32] was used to introduce the dislocation loops in the pristine cells. All dislocation loops were prismatic and of circular shape. Relaxed cells with <100> and ½<111> dislocation loops are shown in Fig. 2a-b, respectively; dislocation loops were detected using the dedicated DXA algorithm [33] of the OVITO software [30]. The various cells containing dislocation loops are listed hereafter:

- In a first set of cells, a single prismatic dislocation loop was introduced in each cell, with a radius varying from 3 up to 35 u.c.; the loop center and the specific Burgers vector were randomly selected.
- In a second set of cells, 20 dislocation loops with random positions were introduced; all 20 loops had the same radius in a given cell, and this radius was varied from 1.2 to 12 u.c.
- In a third set of cells, dislocation loops with a radius of 6 u.c. were randomly inserted in cells in a number from 4 up to 40.

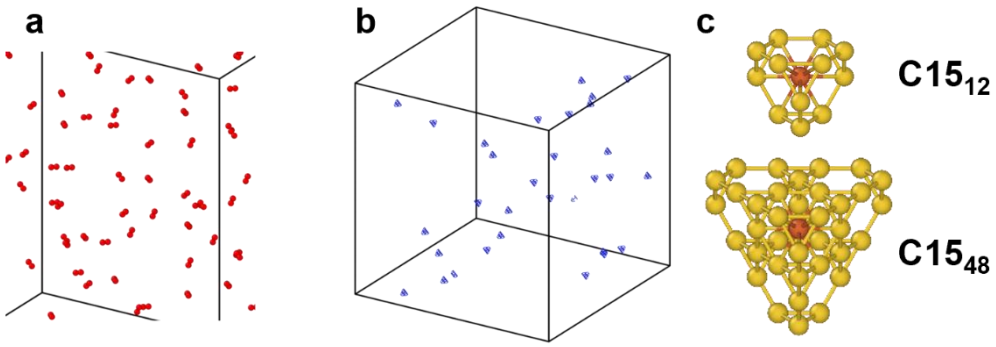


Fig. 1. MD cells containing a) <110> dumbbell SIAs, b) C15 clusters composed of 48 atoms ($C15_{48}$), c) $C15_{12}$ and $C15_{48}$ clusters (the orange sphere represents the central bcc atom). Concentration of extra-atoms in the cells is ~0.02 %.

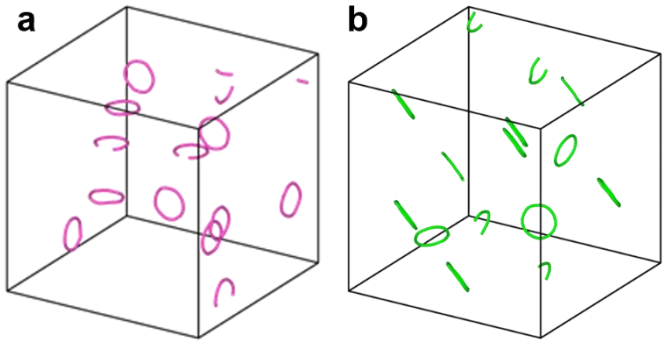


Fig. 2. MD cells containing 12 prismatic a) <100>, b) ½<111> dislocation loops with randomly oriented Burgers vector.

Table 1. Characteristics of the MD cells with interstitial-type defects. N_{extra} is the number of extra-atoms in an MD cell while C_{extra} is their concentration; N_I, R_I and ρ_I refer to the number, radius and density of the different interstitial-type defects, respectively.

<110> dumbbells				
N_{extra}	**C_{extra} (%)**	**ρ_I (nm^{-3})**		
≤ 14336	≤ 1.4	≤ 1.18		
C15 clusters				
Size	**N_I**	**N_{extra}**	**C_{extra} (%)**	**ρ_I (nm^{-3})**
12	≤ 3012	≤ 6024	≤ 0.41	≤ 0.18
48	≤ 598	≤ 5980	≤ 0.41	≤ 0.035
Dislocation loops				
N_I	**R_I (u. c.)**	**N_{extra}**	**C_{extra} (%)**	**ρ_I (nm^{-3})**
1	≤ 35	≤ 7562	≤ 0.74	$8.4x10^{-5}$
20	≤ 12	≤ 15408	≤ 1.5	$1.7x10^{-3}$
≤ 40	6	≤ 8010	≤ 0.78	≤ $3.3x10^{-3}$

2.1.2. Vacancy-type defects

For vacancy-type defects, two configurations were examined: single vacancies, and vacancy clusters in the form of spherical cavities. To form these defects, Fe atoms were removed, which we refer to as *vacant sites* whose number N_{vacant} and concentration C_{vacant} are given in Table 2; also provided in this table are the defect number (N_V), radius (R_V) and density (ρ_V).

Regarding single vacancies, MD cells with a concentration up to 1.4 % were generated by removing randomly selected atoms from a pristine cell. To generate a cavity, all atoms inside a sphere of a given radius, and whose center was randomly selected, were removed. Fig. 3 shows an image of a cell with spherical cavities. Three sets of simulation cells with spherical cavities were produced:

- In a first set of cells, a single cavity was introduced in each cell, with different radii ranging from 0.25 up to 3 nm.
- In a second set of cells, 10 cavities of fixed radius were added in each cell; the radius spanned a range from 0.2 to 1.5 nm in the different cells.
- In a third set of cells, cavities of radius fixed at 1 nm were produced, and their number varied from 1 to up to 30 in the different cells.

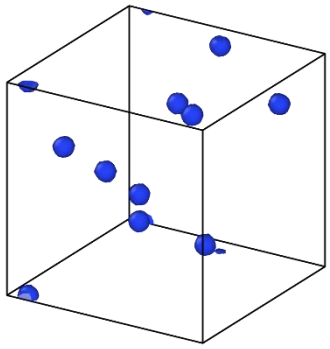


Fig. 3. MD cell containing 10 spherical cavities of radius 1 nm.

Table 2. Characteristics of the MD cells with vacancy-type defects. N_{vacant} is the number of vacant sites in an MD cell while C_{vacant} is their concentration; N_V, R_V and ρ_V refer to the number, radius and density of the different vacancy-type defects, respectively.

Single vacancies		
N_{vacant}	**C_{vacant} (%)**	**ρ_V (nm^{-3})**
≤ 14336	≤ 1.4	≤ 1.18

Cavities				
(N_V)	**R_V (nm)**	**N_{vacant}**	**C_{vacant} (%)**	**ρ_V (nm^{-3})**
1	≤ 3	≤ 9713	≤ 0.95	≤ 8.4×10^{-5}
10	≤ 1.5	≤ 12191	≤ 1.19	8.4×10^{-4}
≤ 30	1	≤ 10836	≤ 1.06	≤ 2.5×10^{-3}

2.1.3. Cell relaxation procedure

A relaxation of the defective (*i.e.,* containing defects) MD cells was required to drive them to a more stable configuration by letting the atoms reach their equilibrium position. Several MD methods have been developed to this end, among which one finds the fast quenching and the conjugate gradient methods [34]. In the present work, a Fortran-based code was used to relax the defective cells by means of the conjugate gradient method. This latter consists in two steps (that can be required or not, depending on the actual cell state): (i) atoms are relocated and (ii) the cell shape is modified. These steps are repeated, according to an iterative process, until both the maximum force F_{max} and stress σ_{max} components converge to pre-defined value. Those values were 1 eV/nm for cells containing Is or Vs, and 0.02 (or 10^{-4}) kbar for cells with Is (or Vs). A lower stress limit was used for cells with Vs so that the cell-shape relaxation process can occur when these defects only were present. Relaxation of the cells was performed under PBCs along the three vectors defining the cell.

2.2. X-ray diffraction simulations

As explained in the next section, to compute the defect relaxation volumes from reciprocal space data, we need to determine the lattice parameter change (hence, the elastic lattice strain) in the defective cells containing. But evaluating, in MD cells, those long-range variations in the crystal periodicity is not a task straightforwardly performed by a direct analysis of the cells, as shown in [3]. To this end, we make use of computational diffraction that allows to carry out this task in the reciprocal space (for details, see [3], [35]). In short, we compute reciprocal space maps (RSMs), that is the diffracted intensity around selected HKL reflections; here, we used the 002 reflection. Two examples of such RSMs are presented in figure 4: Fig. 4a corresponds to a cell containing 36 randomly oriented <100> loops of radius of 6 u.c., and Fig. 4b was calculated from a cell containing 20 ½<111> loops of radius 12 u.c. The monitoring of the position of the reciprocal lattice point (RLP) in the (H,L) planes (*i.e.,* the coordinates of the maximum intensity) allows determining the lattice strain (ε), as this latter reads:

$$\varepsilon = \frac{L_0 - L}{L_0} \qquad \text{Eq. (1)}$$

where L_0 and L are the RLP positions, expressed in reciprocal lattice units (r.l.u.), in pristine and defective cells, respectively. To exclude diffuse scattering that is related to short-range lattice distortions [10,36], only a narrow region around the RLP of a pristine cell was calculated (typically ± 0.02 r.l.u.). To find the accurate position of the RLP, we used a 2D fitting algorithm [3] because simply searching for the pixel of maximum intensity led, in many cases, to inaccurate values. To finish, owing to the finite, relatively small size of the cells (as compared to some defect dimensions), some features in the XRD patterns may arise

because of a pseudo-anisotropy in the defect spatial distribution. To circumvent this issue, RLP positions were averaged over the six different equivalent 002 reflections [3].

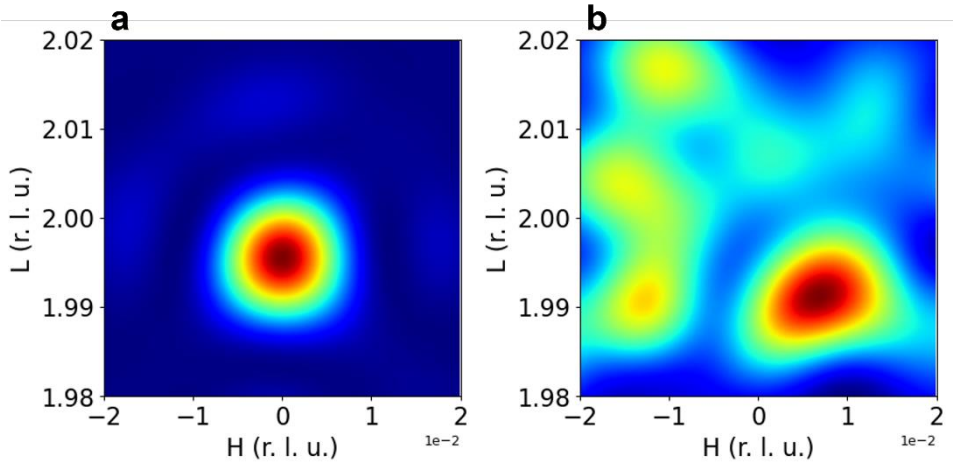


Fig. 4. Computed 002 XRD-RSM of a MD cell containing a) 36 <100> dislocation loops of radius 6 u.c., b) 20 1/2<111> dislocation loops of radius 12 u.c.

2.3. Relaxation volume

In the current work, we used both real and reciprocal space data to determine the relaxation volumes, as explained below.

The volume change related to the creation of a defect in a real crystal involves two distinct contributions: the relaxation volume, V^{rel} and the formation volume, V^{f}. The reader can refer to [37] for a theoretical description of those, and to [38] for a more schematic explanation. Let's here simply recall that, conveniently, one usually considers that the formation of a vacancy implies the displacement of an atom from inside the crystal to the surface, leading to an increase in the crystal volume of one atomic volume (Ω_0). At the same time, in metals, a lattice contraction takes place near the vacancy due to a system equilibration around it. Note that in ionic compounds, where electrostatic interactions can be involved, lattice expansion can take place, but these materials are not the subject of the present paper. This microscopic or lattice volume change is known as the relaxation volume and it may induce the development of a lattice strain, negative in this case. Likewise, the formation of an interstitial defect can be seen as the migration of an atom from the surface to the bulk of the crystal, implying a decrease in volume of Ω_0, while around the interstitial defect a lattice swelling develops, resulting finally in a positive relaxation volume, and hence, possibly, to a tensile lattice strain. The formation volume is then the total volume change resulting from both the volume change at the surface and the relaxation volume around the point defect. The mathematical relationship between V^{rel} and V^{f} is given, for a defect involving N lattice sites, by the following equation:

$$\mathrm{V^f} = \mathrm{V^{rel}} \pm \mathrm{N}\Omega_0 \qquad \text{Eq. (2)}$$

where the - sign holds for Is and the + sign for Vs. The change in the lattice parameter of a crystal (*a*) is connected to V^{rel} while the change in the macroscopic volume (*i.e.,* the crystal volume) is related to V^f. Comparing the relative volume and lattice parameter changes can provide meaningful information on the predominance and concentration of a given (I or V) defect, as demonstrated already in the 1960's [39].

In our simulation cells, there is no surface *per se*, and the defects were generated by injecting or removing atoms at specific locations to produce the desired defect configuration. As the number of lattice sites varies between a pristine cell and one containing defects, the formation volume has no meaning [9]. Therefore, if a change in the MD cell volume occurs, it is entirely related to the relaxation volume that necessarily exists (if the MD cells are relaxed), and both are linked through Eq. (3). Note that in the current work, we will discuss Ω^{rel}, which corresponds to the relaxation volume expressed in atomic volume unit Ω_0, per extra-atom or per vacant site, as this value is easier to discuss because it can be directly compared with Ω_0.

$$\Omega^{rel} = \frac{V^{rel}}{\Omega_0 N_{extra,vacant}} = \frac{\Delta V / V_0}{C_{extra,vacant}} \qquad \text{Eq. (3)}$$

with $\Delta \mathrm{V} = \mathrm{V} - \mathrm{V_0}$, where V_0 and V are the volumes of the relaxed pristine and defective cells, respectively, and $C_{extra,vacant}$ is the concentration of extra-atoms or vacant sites, respectively, as explained in section 2; the atomic volume in Fe is Ω_0 = 0.0233 nm^3 with our interatomic potential.

It must be emphasized that in experiments or for some MD simulation methods of irradiation effects (e.g. when defects form upon Frenkel pair or collision cascade accumulation), V^f can be defined, and in that case, it is usually different from and V^{rel} [40]; for a recent and more detailed discussion about this point, the reader should refer to [9]. So, in many cases, the study of the change in sample or MD cell volume does not allow determining the relaxation volume, but only the formation volume [14]. To circumvent this issue, one can switch from the real space to the reciprocal space, and calculate the lattice strain (ε) from XRD-RSMs of defective cells (or crystals), as explained in section 2.2. Indeed, in that case, the following equation can be applied [10]:

$$\Omega^{rel} = \frac{V^{rel}}{\Omega_0 N_{extra,vacant}} = \frac{3\varepsilon}{C_{extra,vacant}} \qquad \text{Eq. (4)}$$

Note that, strictly speaking, the strain is a 3x3 tensor, $\overline{\overline{\varepsilon}}$. But, as the relaxation volume is related to the diagonal components of this tensor, we are here using a scalar that is $\varepsilon = \left\langle \frac{1}{3} Tr(\overline{\overline{\varepsilon}}) \right\rangle$, the average coming from the fact that we calculated the average of the strain values between the $\langle 00\mathrm{L} \rangle$ directions, as mentioned in the previous section.

It is important to emphasize that the relaxation volumes obtained in the current work correspond to a unique sort of defects, as the cells contain only one defect type at a time (except those in section 4). In addition, as the defect density is varied over a broad range, for many cases, individual strain fields interact, and the corresponding relaxation volume values do integrate these interactions; therefore, there is no need to rely on the usually assumed superposition principle. Consequently, the relaxation volumes determined here can be considered as averaged values over both the different defect spatial configurations and the various defect interactions. To finish, one can mention that Fe is elastically anisotropic. Nonetheless, we used MD cells containing randomly distributed defects with no preferential orientation (except for cells with only one dislocation loop); this situation is more than likely to occur upon irradiation where the defect creation process is usually stochastic. Therefore, the relaxation volumes we obtained can be assumed isotropic (but we did not cancel the elastic anisotropy that is reproduced by the interatomic potential). To support this statement, we verified that the change in the MD cell dimensions consecutive to the injection of defects is the same along the three main directions, which is indeed the case (except when only one defect is present). Note also that we calculated a few RSMs around the 222 reflection (not shown here), and we obtained identical values as for the 002 reflection, again supporting the statement of (apparent) isotropy of the relaxation volumes we derived.

3. Results and discussion

3.1. Defect formation energy

As a preliminary step in the study of the defect relaxation volumes, we start with the analysis of the defect formation energy (E_f) to provide confidence on the methodology we implemented to generate the MD cells containing the defects. Hence, as shown hereafter, we found not only the correct formation energies, but also the expected defect transformation sequence (with increasing defect concentration) previously reported in the literature [31,41], and mentioned in the Introduction. The definition of the formation energy of a defect that we used is the one commonly employed [41], *i.e.,* the difference between the total energy of a cell containing the said defect and the energy of a pristine cell weighted by the relative number of atoms in the two cells:

$$E_f^I = E_{def} - \frac{N_{prist} + N_{extra}}{N_{prist}} E_{prist} \qquad \text{Eq. (5a)}$$

$$E_f^V = E_{def} - \frac{N_{prist} - N_{vacant}}{N_{prist}} E_{prist} \qquad \text{Eq. (5b)}$$

where E_f^I and E_f^V are the formation energies of interstitial and vacancy-type defects, respectively, and N_{prist} is the number of atoms in a pristine MD cell (N_{extra} and N_{vacant} were defined in *sect. 2.1*). E_f^I and E_f^V are here defined for one defect, irrespective of the number of point defects it is composed of. In the following, as for the relaxation volume, we shall present and discuss the formation energies per extra-atom or per vacant site. However, to facilitate the comparison of these energy values with those available in the literature, and to provide additional comments on those, we also give, in Appendix, E_f as a function of the defect size (*i.e.*, N_{extra}/N_I or N_{vacant}/N_V).

Fig. 5a shows the formation energy per extra-atom, $\mathrm{E_f^I/N_{extra}}$, as a function of the extra-atom concentration for the different interstitial-type defects studied. We note that this energy for <110> dumbbell SIAs is the largest one (~3.7 eV) at any extra-atom concentration. This value is slightly lower than the one computed with another interatomic potential (4.3 eV) [42], but similar to those obtained with DFT simulations performed by Domain et al. (3.4 eV) [29] and Chen et al. (3.8 eV) [43]. It is interesting to note that this formation energy for the dumbbells decreases as the extra-atom concentration increases; this feature can most likely be ascribed to defect interactions at high concentration. Yet, this energy remains high, explaining why, above a threshold concentration, dumbbell SIAs agglomerate to form C15 defects, as already reported in [24,44]. Indeed, $\mathrm{E_f^I/N_{extra}}$ for these clusters is less than for the dumbbells, and it is approximately constant throughout the entire investigated concentration range (and

hence, number of defects) for both $C15_{12}$ and $C15_{48}$ clusters. $C15_{12}$ clusters exhibit a larger E_f^I/N_{extra} (3.28 eV) than $C15_{48}$ clusters (1.90 eV), demonstrating that bigger C15 clusters are more stable, in agreement with Zhang et al. results [45]. Besides, E_f^I/N_{extra} for large C15 clusters can be lower than for dislocation loops, as illustrated in Fig. 5a, where is visible a crossover between the formation energy for ½ <111> dislocation loops and $C15_{48}$ clusters (here, below 0.1 % in extra-atom concentration, but this value depends on the defect size). This result confirms that C15 clusters may be more stable than dislocation loops when composed of a few tens of SIAs [31,45], but it is also known that this larger stability of C15 clusters rapidly disappears as the clusters grow further (more than 50 SIAs) [45,46]. To finish, E_f^I/N_{extra} for dislocation loops is the lowest of all the common I-type defects in Fe. This energy, in dislocation loops of fixed size, is constant with C_{extra}, indicating that it does not change with increasing the number of loops of same size. In contrast, it decreases for loops of increasing size, which means that larger loops are more stable. This latter trend is modelled and commented in the Appendix A.

Fig. 5b shows the formation energy per vacant site, E_f^V/N_{vacant}, as a function of the vacant site concentration for the different studied vacancy-type defects. Single vacancies exhibit an E_f^V/N_{vacant} value of around 2.11 eV. Ma et al. [41] and Sivak et al. [42] found very similar values, 2.19 and 1.92 eV, respectively. Domain et al. [29] obtained E_f^V/N_{vacant} of 1.95 eV by DFT calculations, while Soisson et al. [47] reported a value of around 2.2 eV by DFT simulations as well. As expected, E_f^V/N_{vacant} is lower for cavities than it is for single vacancies at any vacant site concentration. For instance, E_f^V/N_{vacant} for cavities of radius 1 nm is only ~0.46 eV, and it is constant regardless of the number of cavities in the cell. Larger cavities exhibit a lower E_f^V/N_{vacant}, as it can be seen in the crossover between E_f^V/N_{vacant} for cavities of increasing size (red line in Fig. 5b) and for cavities of fixed radius 1 nm (green line in Fig. 5b). This last observation confirms that large cavities are more effective at absorbing vacancies as the rate of increase of the formation energy decreases with cavity size, in agreement with [25]. This trend is modelled and commented in the Appendix A.

In conclusion, all energetic characteristics of the model defects we created do compare well with previously reported results in the literature. In addition, we show that the defect formation energies can be summed up when the number of these defects, of fixed size, increases; indeed, the formation energy per extra-atom is (almost) constant over the investigated concentration range (with C_{extra} exceeding ~0.8 % for most of the studied defects). We can now proceed to the determination of the relaxation volume of the various defect types we generated. This is the focus of the next section.

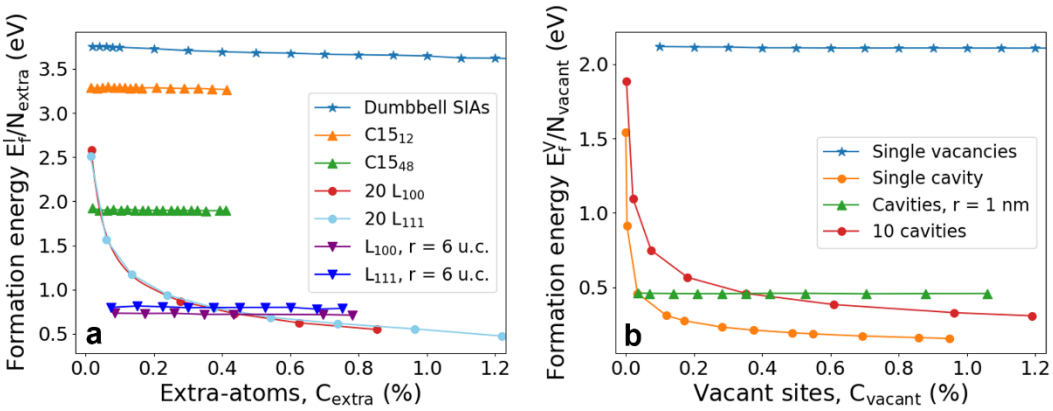


Fig. 5. Defect formation energies. a) Energy of interstitial-type defects per extra-atom (E_f^I/N_{extra}) as a function of the concentration of extra-atoms (C_{extra}). b) Energy of vacancy-type defects per vacant site (E_f^V/N_{vacant}) as a function of the concentration of the vacant sites. Defect types are explicitly mentioned in the figure captions, with L_{100} and L_{111} referring to <100> and ½<111> dislocation loops, respectively. r is the defect radius.

3.2. Relaxation volume of interstitial-type defects

In this section, results concerning the relaxation volume of interstitial-type defects are presented. The different figures display the relaxation volume as a function of both extra-atom concentration and defect radius or density, whether the defects are in fixed number or fixed size, respectively. For instance, Fig. 6a shows the evolution of Ω^{rel} as a function of C_{extra} and of the density of dumbbell SIAs (ρ_I). We can first notice that values obtained through both the XRD calculations and the relative cell volume change (RCVC) are very similar, which was anticipated (see *sect. 2.3*). At the lowest studied defect density, the relaxation volume of the dumbbell SIA is 1.53 Ω_0. This value slightly decreases down to 1.48 Ω_0 at C_{extra} ~0.5 % (density of 0.43 nm^{-3}), where it stabilizes up to a concentration of ~1 %. Then, between 1 and 1.4 %, Ω^{rel} seems to follow a trend of slight increase, which might be due to complex strain field overlapping at such high defect density. But overall, the relaxation volume of the dumbbell SIA does not vary much throughout the broad defect density range that we studied, and it remains at values close to 1.5 Ω_0. Sivak et al. [42] obtained a Ω^{rel} of 1.48 Ω_0 using another EAM potential, while Ma et al. [41] performed DFT simulations and calculated Ω^{rel} to be 1.62 Ω_0. This excellent agreement with other computational approaches supports the validity of our methodology. Regarding C15 clusters (see Fig. 6. b-c), Ω^{rel} values obtained from both XRD and RCVC are practically identical. For the $C15_{12}$ clusters, Ω^{rel} slightly varies between 0.90 Ω_0 and 0.95 Ω_0 at very low defect density 7x10^{-3} nm^{-3} (or C_{extra} ~0.03 %) and then remains constant at 0.91 Ω_0. For the $C15_{48}$ clusters, above 0.1 %, Ω^{rel} is also constant at ~0.98 Ω_0.

Now let us examine the relaxation volume for <100> (referred to as L_{100}) and ½<111> (labeled L_{111}) dislocation loops in cells containing one single defect of varying size; the results are plotted in Fig. 7a and Fig. 8a, respectively. It must be mentioned that the appearance of several pseudo-peaks in the corresponding RSMs prevented a reliable RLP position determination (see *sect. 2.2*). Therefore, for this very case of a single dislocation loop, Ω^{rel} values were determined with the RCVC method only. It can be readily observed that Ω^{rel} exhibits a similar behavior in analogous cells for both loop orientations. A value around 0.95 Ω_0 is obtained for both L_{100} and L_{111} defects. Ω^{rel} is here below the expected 1 Ω_0 value, but a similar result was observed in tungsten MD cells, which is due to the use of an EAM potential [34]. The convergence to Ω_0 per extra-atom in dislocation loops is expected since this object is simply a 2D inclusion of extra-atoms in the crystal. The asymptotic trend towards this value is in fact observed in our simulation results (see blue dashed line in inset in Fig. 7a). Besides, Ω^{rel} in L_{100} defects was fitted to the commonly used equation that relies on the isotropic and anisotropic theory of elasticity to calculate the elastic contribution of the loop to the defect formation energy (see e.g. [31]):

$$\Omega^{rel}/\Omega_0 = 1 + b_0 \frac{lnN_{extra}}{\sqrt{N_{extra}}} + b_1 \frac{1}{\sqrt{N_{extra}}} + \frac{b_2}{N_{extra}} \qquad \text{Eq. (6)}$$

where b_0, b_1 and b_2 are the fitting parameters. An excellent fit is obtained for a concentration of extra-atoms of up to ~0.5 % (corresponding to defects of up to ~5000 atoms), as shown in the inset of Fig. 7a where computed Ω^{rel} (dots) and corresponding fitting curve (dashed line) are plotted. Fitting parameters are given in Table 3.

Table 3. Fitting parameters of the relaxation volume for <100> interstitial dislocation loops (L_{100}) fitted by linear regression to $\Omega^{rel}/\Omega_0 = 1 + b_0 \frac{lnN_{extra}}{\sqrt{N_{extra}}} + b_1 \frac{1}{\sqrt{N_{extra}}} + \frac{b_2}{N_{extra}}$, i.e., Eq. (6). R^2 is the coefficient of determination of the fit.

Dislocation-loop type	Fitting parameters			R^2
	b_0	b_1	b_2	
L_{100}	-1.108 ± 0.068	4.554 ± 0.57	-2.07 ± 2.51	0.971

We now consider cells with 20 loops of a varying size, this latter changing from one cell to the other. Since multiple dislocation loops with randomly oriented Burgers vector were introduced in the cells, the XRD approach exhibits a better reliability as compared to the case of cells with a single loop for which interference fringes in the XRD signal developed because of the anisotropic and non-random strain field around dislocations. These fringes are smoothed out in cells with several defects due to the superposition of the different strain fields from the randomly distributed dislocations. Hence, as shown in Fig. 7b and Fig. 8b, XRD and RCVC provide comparable relaxation volumes. These latter are found

similar to those obtained for cells with only one loop, *i.e.,* ~0.85 Ω_0 and ~0.92 Ω_0 for <100> and ½<111> dislocation loops, respectively. This result also holds for cells with loops of fixed size (namely 6 u.c. or 1.7 nm) but with a varying number of loops (see Fig. 7c and Fig. 8c), for which relaxation volumes are found also very similar: 0.86 Ω_0 and 0.89 Ω_0 for L_{100} and L_{111}, respectively. It is interesting to compare two equivalent (in terms of C_{extra}) simulation cells (per dislocation orientation) generated and relaxed under the same conditions, with (i) a fixed number of loops (see black arrows in Fig. 7b and 8b) on the one side, and (ii) a fixed size (see grey arrows in 7c and 8c) on the other side: the relaxation volumes for the two sets of cells (fixed number *vs* fixed size) are found to be equal (~0.87 Ω_0 as determined with the RCVC method), which is comforting as the cells were generated and analyzed independently.

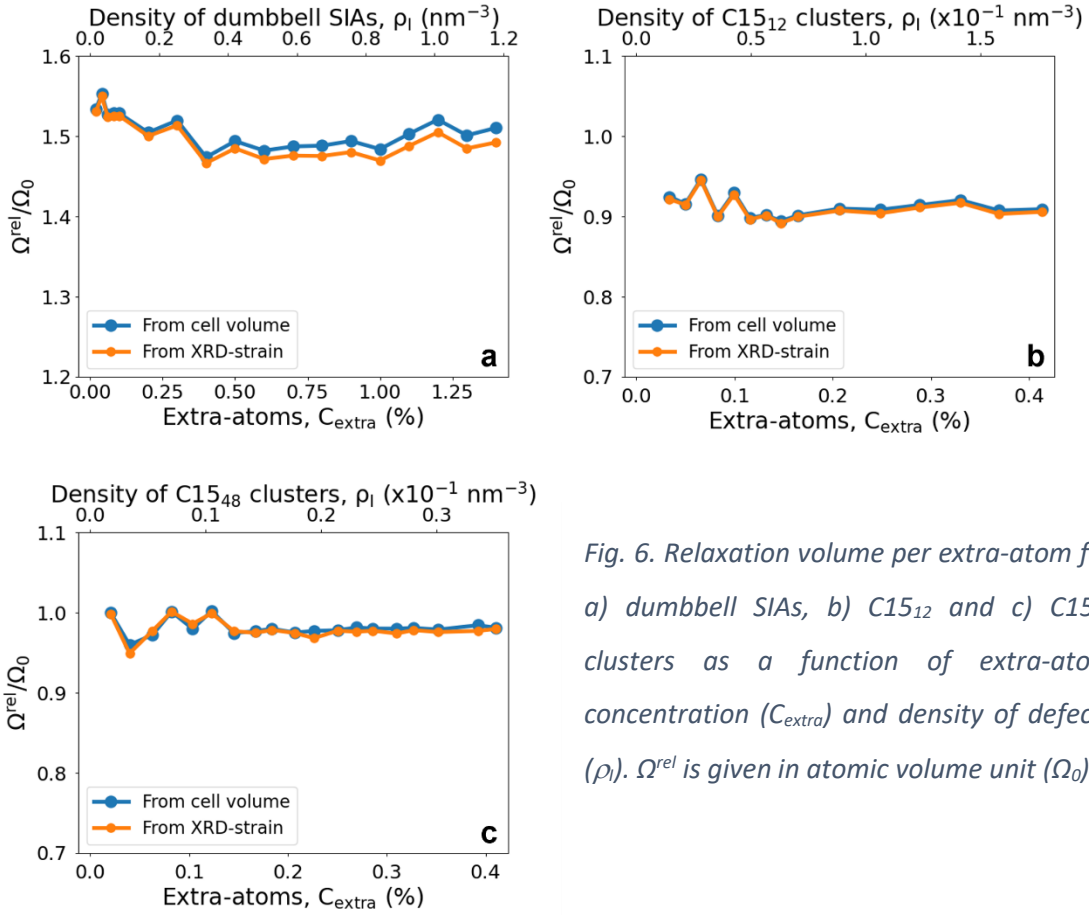


Fig. 6. Relaxation volume per extra-atom for a) dumbbell SIAs, b) $C15_{12}$ and c) $C15_{48}$ clusters as a function of extra-atom concentration (C_{extra}) and density of defects (ρ_I). Ω^{rel} is given in atomic volume unit (Ω_0).

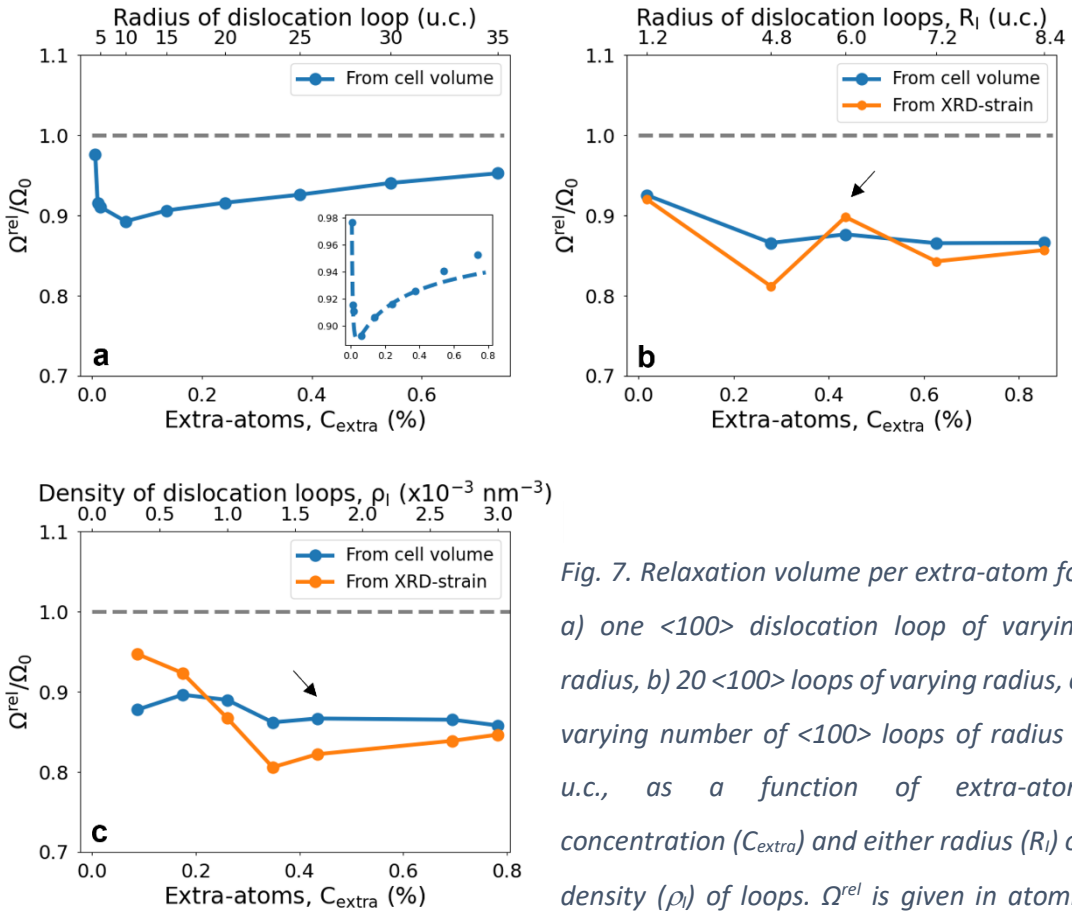


Fig. 7. Relaxation volume per extra-atom for a) one <100> dislocation loop of varying radius, b) 20 <100> loops of varying radius, c) varying number of <100> loops of radius 6 u.c., as a function of extra-atom concentration (C_{extra}) and either radius (R_l) or density (ρ_l) of loops. Ω^{rel} is given in atomic volume unit. Dashed line in inset in Fig. 7a shows Ω^{rel} fitted with Eq. (6). Black arrows point to dots corresponding to two, independent cells with the same defect characteristics (20 <100> dislocation loops of radius 6 u. c.)

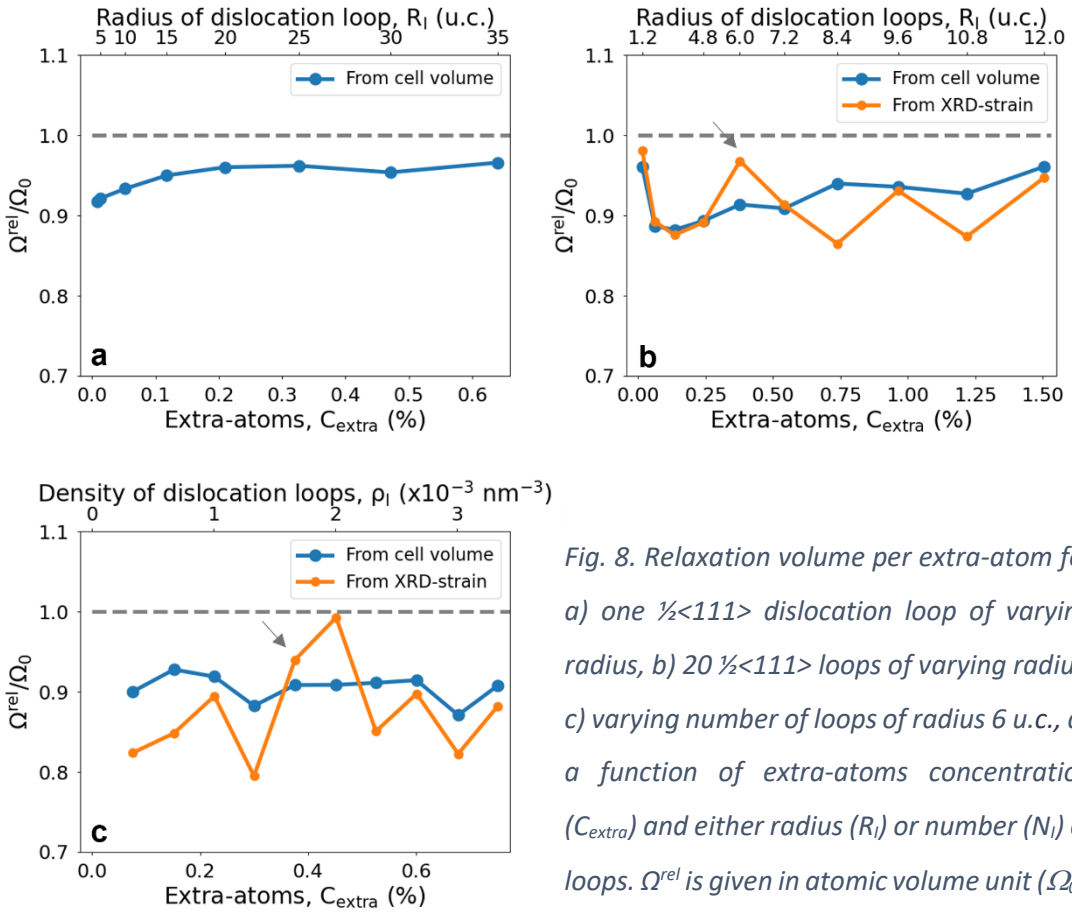


Fig. 8. Relaxation volume per extra-atom for a) one ½<111> dislocation loop of varying radius, b) 20 ½<111> loops of varying radius, c) varying number of loops of radius 6 u.c., as a function of extra-atoms concentration (C_{extra}) and either radius (R_l) or number (N_l) of loops. Ω^{rel} is given in atomic volume unit (Ω_0). Grey arrows point to dots corresponding to two, independent cells with the same defect characteristics (20 <100> dislocation loops of radius 6 u. c.)

3.3. Relaxation volume of vacancy-type defects

The relaxation volume of vacancies in the form of point defects and clusters (spherical cavities) is studied hereafter. As for interstitial defects, Ω^{rel} is presented (in Fig. 9) as a function of the concentration of vacant sites (C_{vacant}) and of either the cavity radius or density. For instance, for single vacancies (Fig. 9a), Ω^{rel} is found to be around -0.11 Ω_0 up to the maximum tested concentration of 1.4 %; both methods (XRD and RCVC) provide identical values. As expected, a vacancy in iron leads to a small lattice contraction, contrary to interstitials that lead to a significant lattice swelling. The current calculated value is half that determined by DFT simulations in bcc iron, *i.e.,* -0.22 Ω_0 [41], but it remains negative and very small. Regarding the cavities, a good agreement is also observed between the relaxation volume values determined from the real space and from the reciprocal space data (*i.e.,* RCVC and XRD, respectively), as shown in Fig. 9b-d. Ω^{rel} values for all cavities are negative. Starting with cells containing a single cavity (see Fig. 9b), Ω^{rel} exhibits a relatively large increase (from -0.09 Ω_0 to ~ -0.015 Ω_0 for the studied cavity sizes) for C_{vacant} lower than 0.1 %, then it slightly increases and asymptotically

approaches 0 when the cavity grows. This result implies that, as the cavity expands by absorbing vacancies, its capacity (per vacant site) to induce a lattice contraction decreases. A same statement holds when there are several cavities, for instance 10, as shown in Fig. 9c. Besides, Fig. 9d indicates that for a fixed radius, Ω^{rel} does not change with varying the defect density. As a consequence, when combining Fig. 9b and Fig. 9c, we get Fig. 9e where data point of Ω^{rel} for one cavity of varying size coincide with those for 10 cavities (of varying size). Therefore, overall, for vacancy-type defects, Ω^{rel} is much more impacted by the defect size than by the defect number.

From these results, we can expect that the relaxation volume tends to 0 for large cavities and to -0.11 Ω_0 (*i.e.,* Ω^{rel} computed for single vacancies) for very small cavities. In fact, the relaxation volume of spherical cavities has been shown to be proportional to $N_{Vacant}^{-1/3}$ (which is usually referred to the "capillary" model), a behavior consistent with our expectations. Ω^{rel} (for a cavity of increasing size) was hence calculated using the following equation:

$$\Omega^{\mathrm{rel}}/\Omega_0 = -\mathrm{s}\mathrm{N}_{\mathrm{vacant}}{}^{-1/3} \qquad \text{Eq. (7)}$$

where *s* is a stress parameter [34] assumed to be 0.11, in order to match, at very small sizes, the relaxation volume we obtained for single vacancies (N_{vacant} = 1). The fitted curve (dashed line in Fig. 9b) shows a very good agreement with the data computed from XRD or RCVC methods (symbols in Fig. 9b). Eq. (7) was also used to successfully fit the Ω^{rel} data for cells with 10 cavities (of varying size); results are plotted in Fig. 9c. The agreement between the fitted curves obtained with Eq. (7) and the computed data for the two cases (Fig. 9b and Fig. 9c) demonstrates that the whole relaxation volumes we determined constitutes a consistent set of results; otherwise, using another value for the *s* parameter would have not led to an agreement at all. To finish, one must mention that if cavities lead to nearly no change in the lattice volume (and hence, in the lattice parameter), they are at the origin of the so-called "void swelling" that can occur in irradiated metals [9], [48]; both should not be mixed up.

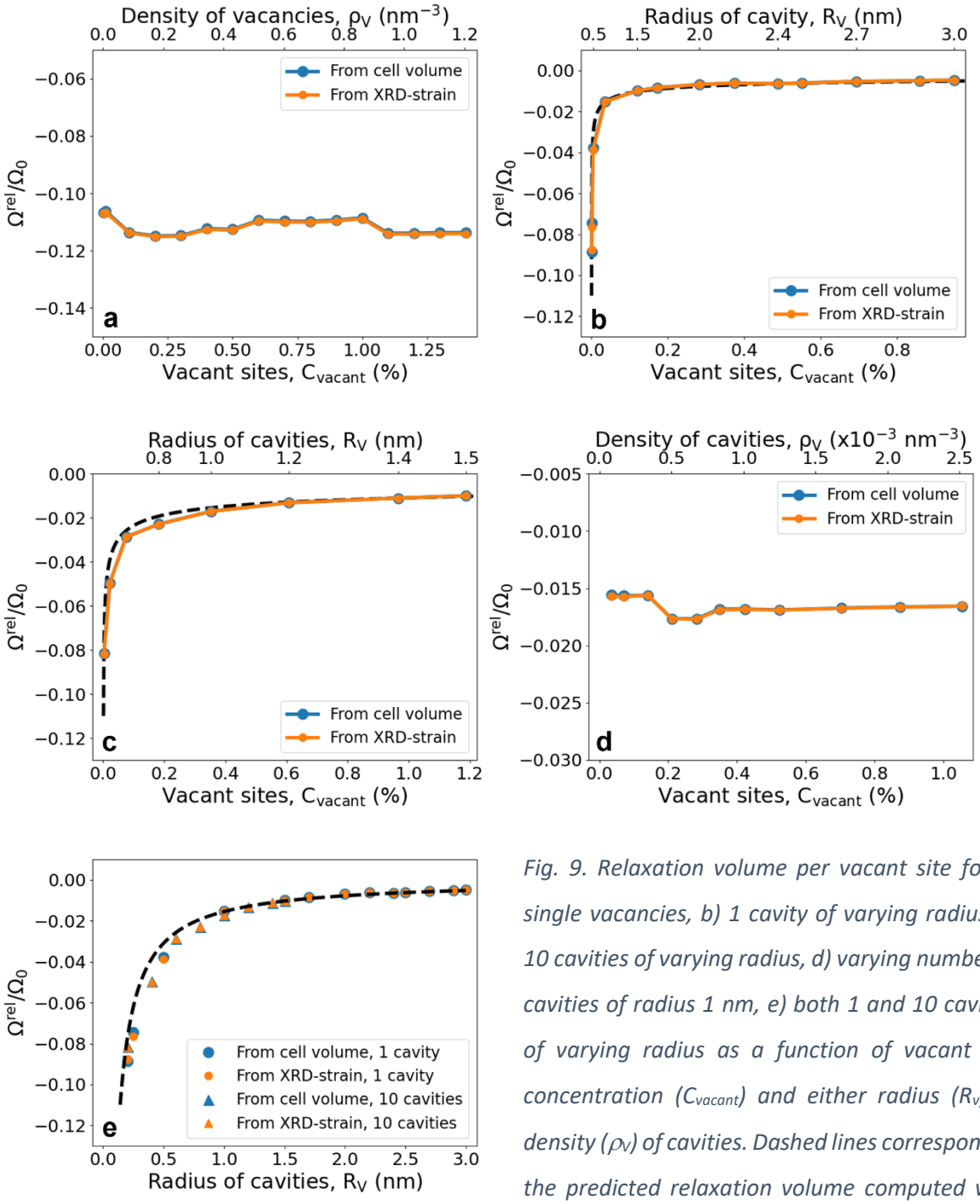


Fig. 9. Relaxation volume per vacant site for a) single vacancies, b) 1 cavity of varying radius, c) 10 cavities of varying radius, d) varying number of cavities of radius 1 nm, e) both 1 and 10 cavities of varying radius as a function of vacant site concentration (C_{vacant}) and either radius (R_v) or density (ρ_V) of cavities. Dashed lines correspond to the predicted relaxation volume computed with Eq. (7). Ω^{rel} is given in atomic volume unit (Ω_0).

3.4. Additivity of the relaxation volumes

In the previous section, we showed that the relaxation volumes for individual defects can be added when the defect size and/or number increases. Indeed, except for very small cavities or when a single defect is considered, Ω^{rel} is independent of defect radius and density. Now the question that naturally arises is the following: do these quantities also simply add-up when several defects co-exist and potentially interact? To answer this question, we created MD cells containing several defect types; the corresponding defect combinations correspond to microstructures than can be observed in irradiated Fe samples (below 400°C). The detailed cell characteristics are provided in Table 4. Below is given a brief description of these cells:

- A cell with a concentration of 0.28 % of both dumbbell SIAs and monovacancies, labelled I&V.
- A cell with 40 1/2<111> dislocation loops of radius 6 u.c. and 0.7 % of single vacancies, labelled L_{111}&V.
- A cell with 40 1/2<111> dislocation loops of radius 6 u.c. and 5 <100> dislocation loops of radius 6 u.c.; this cell is referred to as L_{111}&L_{100}.
- A cell with 40 1/2<111> dislocation loops of radius 6 u.c., 5 <100> dislocation loops of radius 6 u.c. and 0.7 % of single vacancies; this cell is named L&V, and it is illustrated in Fig. 10.

Table 4. Characteristics of the MD cells with different types of defects. The '&' symbol stands for 'and', and the '/' symbol is used to separate the characteristics of the ½<111> dislocation loops (L_{111}) from those of the <100> loops (L_{100}), that is, left side for L_{111} and right side for L_{100}.

	N_I & N_V	R_I & R_V (u. c.)	N_{extra} & N_{vacant}	C_{extra} & C_{vacant} (%)	ρ_I & ρ_V (nm^{-3})
I&V	2895 & 2895	-	2895 & 2895	0.28 & 0.28	0.242 & 0.24
L_{111}&V	40 & 7168	6 & -	7694 & 7168	0.75 & 0.70	$3.3x10^{-3}$ & 0.60
L_{111}&L_{100}	40 & 5	6 & 6	7694 & 1113	0.75 & 0.11	$3.3x10^{-3}$ & $4.2x10^{-4}$
L&V	40 / 5 & 7168	6 / 6 & -	7694 / 1113 & 7168	0.75 / 0.11 & 0.70	$3.3x10^{-3}$ / $4.2x10^{-4}$ & 0.60

After relaxation of the MD cells, we used the Wigner-Seitz [49] analysis proposed in the Ovito software [30] to count the effective numbers of Is and Vs in the cells, and we found the nominal values. Note that we previously verified that this analysis provides correct values in our model cells, *i.e.,* in those containing only one type of defects (but it does not work for C_{15} clusters). Knowing the concentration of extra-atoms and vacant sites, and using the appropriate relaxation volumes, we calculated the predicted changes in lattice parameter using the following relationship:

$$\varepsilon_{predicted} = \sum_{Is,Vs} \frac{1}{3} c_{extra,vacant} \Omega^{rel}_{I,V} \qquad \text{Eq. (8)}$$

We then compared these values with those (ε_{MD-XRD}) we actually determined from computational XRD performed on the MD cells listed in Table 4. Results are given in Table 5. It readily appears that there is an excellent agreement between predicted and XRD computed values, the difference between the two being less than 2 %, which is typically the standard deviation we have on the relaxation volume values. This agreement also holds for the change in the cell volume (not shown here), with an even better accuracy as the standard deviation is lower for the corresponding Ω^{rel} values. Consequently, it can be safely assumed that summing the different relaxation volumes provides reasonable estimates of the overall change in the lattice parameter, and also, when applicable [9], in the macroscopic volume change. This additivity can hence be safely used in mesoscale models such as object kinetic Monte Carlo or cluster dynamics simulations, and also to derive defect concentrations from experimental strain measurements in actual irradiated crystals. This result also confirms, if it were necessary, that using elasticity theory to characterize and describe defects through their elastic dipole tensor is a valid approach.

Table 5: Predicted strain level ($\varepsilon_{predicted}$) using the relaxation volumes (Ω^{rel}) found in this work and the defect concentrations given in Table 4, and the actual strain (ε_{MD-XRD}) as determined by computational XRD on the MD cells presented in Table 4; the difference between the two strain values is also provided. The '&' symbol stands for 'and', and the '/' symbol is used to separate the characteristics of the ½<111> dislocation loops (L_{111}) from those of the <100> loops (L_{100}), that is, left side for L_{111} and right side for L_{100}.

	I&V	L_{111}&V	L_{111}&L_{100}	L_s&V
Ω^{rel} (Ω_0)	1.5 & -0.11	0.905 & -0.11	0.905 & 0.873	0.905 / 0.873 & -0.11
$\varepsilon_{predicted}$ (%)	0.131	0.201	0.258	0.232
ε_{MD-XRD} (%)	0.129	0.198	0.259	0.237
difference (%)	1.5	1.5	0.4	2

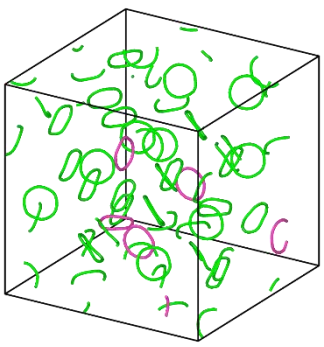


Fig. 10. MD cell containing prismatic <100> (pink) and ½<111> (green) dislocation loops with randomly oriented Burgers vector.

4. Conclusion

To summarize, in this work, we developed an *in silico* approach to determine the relaxation volume (per extra-atom or vacant site), here called Ω^{rel}, of crystalline defects commonly observed in bcc Fe. We first created MD cells containing a unique type of defects, the size and density of which were perfectly controlled, and we verified that the defect formation energies exhibited consistent values and evolution with respect to experimental and computed results available in the literature. Second, we performed a dual calculation of the relaxation volumes, using both real space and reciprocal space data. More precisely, for the former, we computed the change in the MD cell dimensions. For the latter, we implemented a computational diffraction method to generate 2D-XRD maps of the scattered intensity arising from the MD cells; Ω^{rel} values were then computed from the (elastic) lattice strain derived from the analysis of the XRD signals. Our main results put forward that <110> dumbbell SIAs have the largest Ω^{rel} (~1.5 Ω_0). C15 clusters showed a lower Ω^{rel} than the dumbbell SIAs, and slightly different values for the two studied cluster sizes were found: ~0.91 Ω_0 for $C15_{12}$ and ~0.98 Ω_0 for $C15_{48}$. Both ½<111> and <100> interstitial dislocation loops exhibit a relaxation volume per extra-atom close to one atomic volume, ~0.905 Ω_0 and ~0.873 Ω_0, respectively; although both values appear to be very close, one should prefer to discriminate the two, because predicted lattice strain using these Ω^{rel} values can have a higher accuracy than this difference between the two dislocation orientations. Regarding vacancy-type defects, single vacancies are characterized by the smallest Ω^{rel} (~-0.11 Ω_0). This latter exhibit, for cavities, an asymptotic behavior with increasing defect size and hence tends to zero for large clusters.

Using these Ω^{rel} values, we predicted the lattice strain in MD cells containing several types of defects. We showed that the relaxation volumes can be summed up to precisely (within 2 %) estimate the change in the lattice parameter. The relaxation volumes that we here provide can finally be used to feed larger-scale simulation models such as cluster dynamics. Moreover, the proposed methodology can be applied to any other single or multi-elemental material, providing the defect creation process is well controlled. One can cite in particular concentrated solid solution and high-entropy alloys which are currently attracting a lot of interest and for which multi-scale modelling and experimental data are required [50,51].

Acknowledgments

This work has been carried out within the framework of the French Federation for Fusion FR-FCM and the Training and Education WP of the EUROfusion Consortium, funded by the European Union via the Euratom Research and Training Programme (Grant Agreement No 101052200 — EUROfusion). Views and opinions expressed are however those of the author(s) only and do not necessarily reflect those of the European Union or the European Commission. Neither the European Union nor the European Commission can be held responsible for them. Part of this work has been funded by the NEEDS program of the CNRS, within the RAISIN mater project. This project has also received financial support from the CNRS through the 80|Prime program.

Data availability statement

Data will be shared upon request.

References

[1] J.-P. Crocombette, F. Willaime, Ab Initio Electronic Structure Calculations for Nuclear Materials, in: Compr. Nucl. Mater., Elsevier, 2020: pp. 517–543. https://doi.org/10.1016/B978-0-12-803581-8.00658-5.

[2] M.J. Gillan, The long-range distortion caused by point defects, Philos. Mag. A. 48 (1983) 903–919. https://doi.org/10.1080/01418618308244326.

[3] A. Boulle, A. Chartier, A. Debelle, X. Jin, J.-P. Crocombette, Computational diffraction reveals long-range strains, distortions and disorder in molecular dynamics simulations of irradiated single crystals, J. Appl. Crystallogr. 55 (2022) 296–309. https://doi.org/10.1107/S1600576722001406.

[4] P.H. Dederichs, C. Lehmann, H.R. Schober, A. Scholz, R. Zeller, Lattice theory of point defects, J. Nucl. Mater. 69–70 (1978) 176–199. https://doi.org/10.1016/0022-3115(78)90243-X.

[5] J.D. Eshelby, The Continuum Theory of Lattice Defects, in: Solid State Phys., 1956: pp. 79–144. https://doi.org/10.1016/S0081-1947(08)60132-0.

[6] W. Jäger, P. Ehrhart, W. Schilling, Dislocation Patterning under Irradiation, Solid State Phenom. 3–4 (1991) 279–294. https://doi.org/10.4028/www.scientific.net/SSP.3-4.279.

[7] S.J. Zinkle, Radiation-induced effects on microstructure, in: Compr. Nucl. Mater., 1st ed., Elsevier Inc., 2012: pp. 65–98. https://doi.org/10.1016/B978-0-08-056033-5.00003-3.

[8] S.L. Dudarev, D.R. Mason, E. Tarleton, P.W. Ma, A.E. Sand, A multi-scale model for stresses, strains and swelling of reactor components under irradiation, Nucl. Fusion. 58 (2018). https://doi.org/10.1088/1741-4326/aadb48.

[9] T. Jourdan, M. Nastar, On the relative contributions of point defect clusters to macroscopic swelling of metals, J. Appl. Phys. 131 (2022) 225103. https://doi.org/10.1063/5.0094189.

[10] P. Ehrhart, Investigation of radiation damage by X-ray diffraction, J. Nucl. Mater. 216 (1994) 170–198. https://doi.org/10.1016/0022-3115(94)90012-4.

[11] D. Bachiller-Perea, A. Debelle, L. Thomé, J.P. Crocombette, Study of the initial stages of defect generation in ion-irradiated MgO at elevated temperatures using high-resolution X-ray diffraction, J. Mater. Sci. 51 (2016) 1456–1462. https://doi.org/10.1007/s10853-015-9465-3.

[12] D.R. Mason, S. Das, P.M. Derlet, S.L. Dudarev, A.J. London, H. Yu, N.W. Phillips, D. Yang, K. Mizohata, R. Xu, F. Hofmann, Observation of Transient and Asymptotic Driven Structural States of Tungsten Exposed to Radiation, Phys. Rev. Lett. 125 (2020) 225503. https://doi.org/10.1103/PhysRevLett.125.225503.

[13] D.J. Bacon, D.M. Barnett, R.O. Scattergood, Anisotropic continuum theory of lattice defects, Prog. Mater. Sci. 23 (1980) 51–262. https://doi.org/10.1016/0079-6425(80)90007-9.

[14] G.Leibried, N. Breuer, Point Defects in Metals I, Springer-Verlag, Berlin/Heidelberg, 1978. https://doi.org/10.1007/BFb0045966.

[15] C. Varvenne, F. Bruneval, M.C. Marinica, E. Clouet, Point defect modeling in materials: Coupling ab initio and elasticity approaches, Phys. Rev. B - Condens. Matter Mater. Phys. 88 (2013) 1–7. https://doi.org/10.1103/PhysRevB.88.134102.

[16] C. Varvenne, E. Clouet, Elastic dipoles of point defects from atomistic simulations, Phys. Rev. B. 96 (2017) 1–11. https://doi.org/10.1103/PhysRevB.96.224103.

[17] E. Clouet, C. Varvenne, T. Jourdan, Elastic modeling of point-defects and their interaction, Comput. Mater. Sci. 147 (2018) 49–63. https://doi.org/10.1016/j.commatsci.2018.01.053.

[18] J.S. Wróbel, M.R. Zemła, D. Nguyen-Manh, P. Olsson, L. Messina, C. Domain, T. Wejrzanowski, S.L. Dudarev, Elastic dipole tensors and relaxation volumes of point defects in concentrated random magnetic Fe-Cr alloys, Comput. Mater. Sci. 194 (2020) 110435. https://doi.org/10.1016/j.commatsci.2021.110435.

[19] S.J. Zinkle, J.T. Busby, Structural materials for fission & fusion energy, Mater. Today. 12 (2009) 12–19. https://doi.org/10.1016/S1369-7021(09)70294-9.

[20] J. Marian, B.D. Wirth, R. Schäublin, G.R. Odette, J.M. Perlado, MD modeling of defects in Fe and their interactions, J. Nucl. Mater. 323 (2003) 181–191. https://doi.org/10.1016/j.jnucmat.2003.08.037.

[21] L. Malerba, N. Anento, J.P. Balbuena, C.S. Becquart, N. Castin, M.J. Caturla, C. Domain, C. Guerrero, C.J. Ortiz, B. Pannier, A. Serra, Physical mechanisms and parameters for models of microstructure evolution under irradiation in Fe alloys – part I: pure Fe, Nucl. Mater. Energy. 29 (2021) 101069. https://doi.org/10.1016/j.nme.2021.101069.

[22] Z. Yao, M.L. Jenkins, M. Hernández-Mayoral, M.A. Kirk, The temperature dependence of heavy-ion damage in iron: A microstructural transition at elevated temperatures, Philos. Mag. 90 (2010) 4623–4634. https://doi.org/10.1080/14786430903430981.

[23] M. Roldán, F.J. Sánchez, P. Fernández, C.J. Ortiz, A. Gómez-herrero, D.J. Rey, Dislocation loop generation differences between thin films and bulk in EFDA pure iron under self-ion irradiation at 20 MeV, Metals (Basel). 11 (2021). https://doi.org/10.3390/met11122000.

[24] M.C. Marinica, F. Willaime, J.P. Crocombette, Irradiation-induced formation of nanocrystallites with C15 laves phase structure in bcc iron, Phys. Rev. Lett. 108 (2012) 1–5. https://doi.org/10.1103/PhysRevLett.108.025501.

[25] M.R. Gilbert, S.L. Dudarev, P.M. Derlet, D.G. Pettifor, Structure and metastability of mesoscopic vacancy and interstitial loop defects in iron and tungsten, J. Phys. Condens. Matter. 20 (2008) 345214. https://doi.org/10.1088/0953-8984/20/34/345214.

[26] J.J. de Pablo, N.E. Jackson, M.A. Webb, L.-Q. Chen, J.E. Moore, D. Morgan, R. Jacobs, T. Pollock,

D.G. Schlom, E.S. Toberer, J. Analytis, I. Dabo, D.M. DeLongchamp, G.A. Fiete, G.M. Grason, G. Hautier, Y. Mo, K. Rajan, E.J. Reed, E. Rodriguez, V. Stevanovic, J. Suntivich, K. Thornton, J.-C. Zhao, New frontiers for the materials genome initiative, Npj Comput. Mater. 5 (2019) 41. https://doi.org/10.1038/s41524-019-0173-4.

[27] M.R. Gilbert, K. Arakawa, Z. Bergstrom, M.J. Caturla, S.L. Dudarev, F. Gao, A.M. Goryaeva, S.Y. Hu, X. Hu, R.J. Kurtz, A. Litnovsky, J. Marian, M.-C. Marinica, E. Martinez, E.A. Marquis, D.R. Mason, B.N. Nguyen, P. Olsson, Y. Osetskiy, D. Senor, W. Setyawan, M.P. Short, T. Suzudo, J.R. Trelewicz, T. Tsuru, G.S. Was, B.D. Wirth, L. Yang, Y. Zhang, S.J. Zinkle, Perspectives on multiscale modelling and experiments to accelerate materials development for fusion, J. Nucl. Mater. 554 (2021) 153113. https://doi.org/10.1016/j.jnucmat.2021.153113.

[28] L. Malerba, M.C. Marinica, N. Anento, C. Björkas, H. Nguyen, C. Domain, F. Djurabekova, P. Olsson, K. Nordlund, A. Serra, D. Terentyev, F. Willaime, C.S. Becquart, Comparison of empirical interatomic potentials for iron applied to radiation damage studies, J. Nucl. Mater. 406 (2010) 19–38. https://doi.org/10.1016/j.jnucmat.2010.05.017.

[29] C. Domain, C.S. Becquart, Ab initio calculations of defects in Fe and dilute Fe-Cu alloys, Phys. Rev. B. 65 (2001) 024103. https://doi.org/10.1103/PhysRevB.65.024103.

[30] A. Stukowski, Visualization and analysis of atomistic simulation data with OVITO–the Open Visualization Tool, Model. Simul. Mater. Sci. Eng. 18 (2010) 015012. https://doi.org/10.1088/0965-0393/18/1/015012.

[31] R. Alexander, M.C. Marinica, L. Proville, F. Willaime, K. Arakawa, M.R. Gilbert, S.L. Dudarev, Ab initio scaling laws for the formation energy of nanosized interstitial defect clusters in iron, tungsten, and vanadium, Phys. Rev. B. 94 (2016) 1–15. https://doi.org/10.1103/PhysRevB.94.024103.

[32] E. Clouet, Babel Software, (n.d.). http://emmanuel.clouet.free.fr/Programs/Babel/index.html.

[33] A. Stukowski, V. V. Bulatov, A. Arsenlis, Automated identification and indexing of dislocations in crystal interfaces, Model. Simul. Mater. Sci. Eng. 20 (2012) 085007. https://doi.org/10.1088/0965-0393/20/8/085007.

[34] D.R. Mason, D. Nguyen-Manh, M.C. Marinica, R. Alexander, A.E. Sand, S.L. Dudarev, Relaxation volumes of microscopic and mesoscopic irradiation-induced defects in tungsten, J. Appl. Phys. 126 (2019). https://doi.org/10.1063/1.5094852.

[35] X. Jin, A. Boulle, A. Chartier, J.P. Crocombette, A. Debelle, Analysis of strain and disordering kinetics based on combined RBS-channeling and X-ray diffraction atomic-scale modelling, Acta Mater. 201 (2020) 63–71. https://doi.org/10.1016/j.actamat.2020.09.076.

[36] R.J. Olsen, K. Jin, C. Lu, L.K. Beland, L. Wang, H. Bei, E.D. Specht, B.C. Larson, Investigation of defect clusters in ion-irradiated Ni and NiCo using diffuse X-ray scattering and electron microscopy, J. Nucl. Mater. 469 (2016) 153–161. https://doi.org/10.1016/j.jnucmat.2015.11.030.

[37] M.J. Gillan, The volume of formation of defects in ionic crystals, Philos. Mag. A. 43 (1981) 301–312. https://doi.org/10.1080/01418618108239410.

[38] J. Friedel, Défauts ponctuels dans les métaux, J. Phys. 24 (1963) 417–425. https://doi.org/10.1051/jphys:01963002407041700.

[39] R.O. Simmons, R.W. Balluffi, Measurements of Equilibrium Vacancy Concentrations in Aluminum, Phys. Rev. 117 (1960) 52–61. https://doi.org/10.1103/PhysRev.117.52.

[40] L. Van Brutzel, P. Fossati, A. Chartier, Molecular dynamics simulations of microstructural evolution of irradiated (U,Pu)O_2 studied via simulated XRD patterns, J. Nucl. Mater. 567 (2022)

153834. https://doi.org/10.1016/j.jnucmat.2022.153834.

[41] P.W. Ma, S.L. Dudarev, Universality of point defect structure in body-centered cubic metals, Phys. Rev. Mater. 3 (2019) 1–16. https://doi.org/10.1103/PhysRevMaterials.3.013605.

[42] A.B. Sivak, V.M. Chernov, N.A. Dubasova, V.A. Romanov, Anisotropy migration of self-point defects in dislocation stress fields in BCC Fe and FCC Cu, J. Nucl. Mater. 367-370 A (2007) 316–321. https://doi.org/10.1016/j.jnucmat.2007.03.134.

[43] Z. Chen, N. Kioussis, N. Ghoniem, D. Seif, Strain-field effects on the formation and migration energies of self interstitials in α-Fe from first principles, Phys. Rev. B - Condens. Matter Mater. Phys. 81 (2010) 1–10. https://doi.org/10.1103/PhysRevB.81.094102.

[44] L. Dézerald, M.C. Marinica, L. Ventelon, D. Rodney, F. Willaime, Stability of self-interstitial clusters with C15 Laves phase structure in iron, J. Nucl. Mater. 449 (2014) 219–224. https://doi.org/10.1016/j.jnucmat.2014.02.012.

[45] Y. Zhang, X.M. Bai, M.R. Tonks, S.B. Biner, Formation of prismatic loops from C15 Laves phase interstitial clusters in body-centered cubic iron, Scr. Mater. 98 (2015) 5–8. https://doi.org/10.1016/j.scriptamat.2014.10.033.

[46] A. Chartier, M.C. Marinica, Rearrangement of interstitial defects in alpha-Fe under extreme condition, Acta Mater. 180 (2019) 141–148. https://doi.org/10.1016/j.actamat.2019.09.007.

[47] F. Soisson, C.C. Fu, Cu-precipitation kinetics in α-Fe from atomistic simulations: Vacancy-trapping effects and Cu-cluster mobility, Phys. Rev. B - Condens. Matter Mater. Phys. 76 (2007) 1–12. https://doi.org/10.1103/PhysRevB.76.214102.

[48] L.K. Mansur, Void Swelling in Metals and Alloys Under Irradiation: An Assessment of the Theory, Nucl. Technol. 40 (1978) 5–34. https://doi.org/10.13182/NT78-2.

[49] K. Nordlund, M. Ghaly, R.S. Averback, M. Caturla, T. Diaz de la Rubia, J. Tarus, Defect production in collision cascades in elemental semiconductors and fcc metals, Phys. Rev. B. 57 (1998) 7556–7570. https://doi.org/10.1103/PhysRevB.57.7556.

[50] M. Beyramali Kivi, Y. Hong, M. Asle Zaeem, A Review of Multi-Scale Computational Modeling Tools for Predicting Structures and Properties of Multi-Principal Element Alloys, Metals (Basel). 9 (2019) 254. https://doi.org/10.3390/met9020254.

[51] G. Velişa, Z. Fan, M.L. Crespillo, H. Bei, W.J. Weber, Y. Zhang, Temperature effects on damage evolution in ion-irradiated NiCoCr concentrated solid-solution alloy, J. Alloys Compd. 832 (2020) 154918. https://doi.org/10.1016/j.jallcom.2020.154918.

[52] N. Soneda, T.D. de la Rubia, Defect production, annealing kinetics and damage evolution in α-Fe: An atomic-scale computer simulation, Philos. Mag. A. 78 (1998) 995–1019. https://doi.org/10.1080/01418619808239970.

Appendix A

To provide a more complete data set of the defect characteristics, we modelled the trends in the defect energetics we observed applying commonly used equations to fit the formation energies. For interstitial dislocation loops, we applied the following analytical relationship that relies on the isotropic and anisotropic theory of elasticity to calculate the elastic contribution of the loop to E_f^I (see e.g. [31]):

$$E_f^I = a_0\sqrt{N_{extra}}lnN_{extra} + a_1\sqrt{N_{extra}} + a_2 \qquad \text{Eq. (A1)}$$

where N_{extra} is the number of interstitials, and a_0, a_1 and a_2 are the fitting parameters. The fitted curves for <100> and ½<111> dislocation loops are presented in Fig. A1-a and Fig. A1-b, respectively, and the fitting parameters are given in Table A1. An excellent agreement is obtained up to ~6000 interstitials for both types of dislocation loops. Regarding the formation energy of a single cavity, it was fitted to the popular "capillary" model [52]:

$$E_f^V = a_0{N_{vacant}}^{2/3} + a_1 \qquad \text{Eq. (A2)}$$

The resulting fitted curve is shown in Fig. A1-c, and the fitting parameters are given in Table A2. A good agreement is obtained over the whole studied defect concentration range.

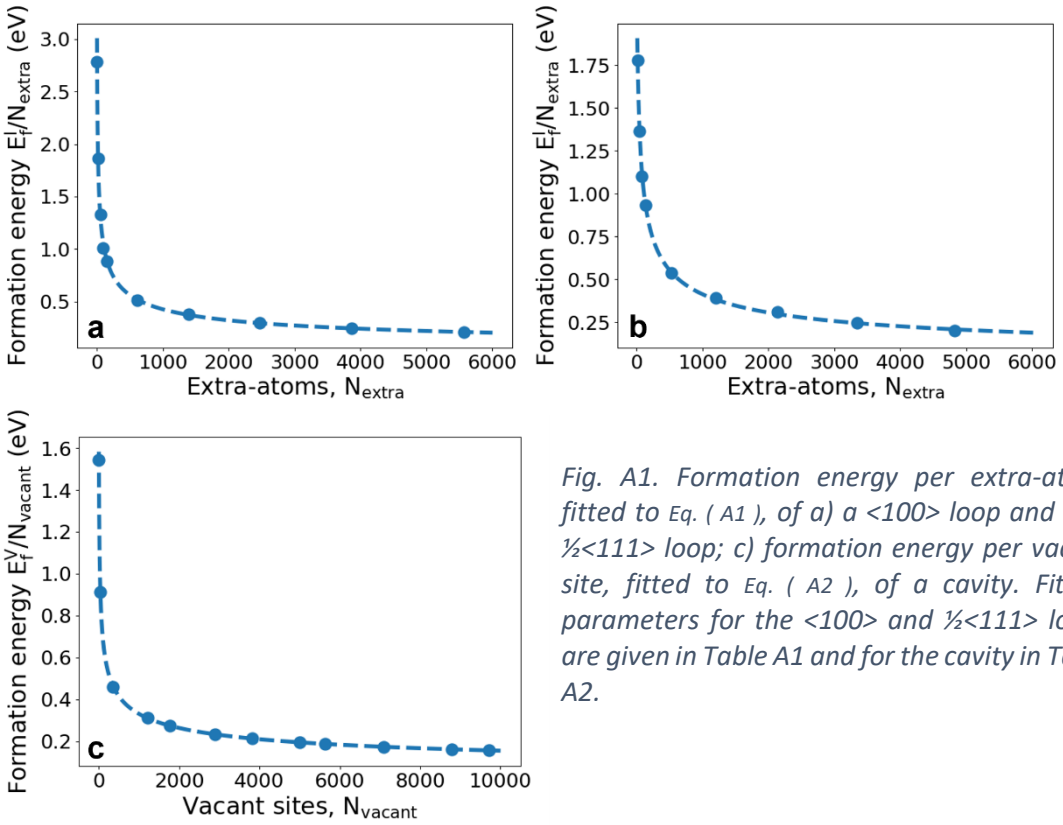


Fig. A1. Formation energy per extra-atom, fitted to Eq. (A1), of a) a <100> loop and b) a ½<111> loop; c) formation energy per vacant site, fitted to Eq. (A2), of a cavity. Fitting parameters for the <100> and ½<111> loops are given in Table A1 and for the cavity in Table A2.

Table A1. Fitting parameters of the formation energy of a single loop fitted by linear regression to $E_f^I = a_0\sqrt{N_{extra}}lnN_{extra} + a_1\sqrt{N_{extra}} + a_2$. *$R^2$ is the coefficient of determination of the fit.*

Dislocation-loop type	Fitting parameters			R^2
	a_0	a_1	a_2	
<100>	1.290 ± 0.097	4.599 ± 0.731	0.112 ± 1.817	0.998
½<111>	0.737 ± 0.209	8.335 ± 1.687	-11.416 ± 5.977	0.999

Table A2. Fitting parameters of the formation energy of a single cavity fitted by linear regression to $E_f^V = a_0 {N_{vacant}}^{2/3} + a_1$. *R^2 is the coefficient of determination of the fit.*

Fitting parameters		R^2
a_0	a_1	
3.32 ± 0.004	-1.774 ± 0.978	0.999

Showing the formation energy as a function of the concentration of extra-atoms or vacant sites (Fig.5) could lead to the misleading conclusion that changes in E_f are exclusively due to changes in the defect concentration. But in fact, the most important factor is the defect size. To show more conveniently the effect of this parameter on the defect formation energy, in Fig. A2 is plotted E_f per extra-atom or vacant site and per defect number, that is, N_{extra}/N_I or N_{vacant}/N_V, respectively (in other words, E_f is plotted as a function of the defect size expressed by the number of point defects they contain). The hierarchy in

defect formation energy observed in Fig.5 is obviously maintained. More importantly, for interstitials, we can see that E_f coincides for dislocation loops of fixed radius (6 u.c.) in MD cells containing 4 loops (upside down triangle dots in Fig. A2a) and 20 loops (solid lines in Fig. A2a); this result indicates that the defect size is the most important parameter regarding the formation energy (except for dumbbells at high concentration, as explained in section 3.1). This statement holds for the vacancy-type defects, as it can clearly be observed in Fig. A2b that the energy curves and data points coincide when the defects have the same size, irrespective of their number (at least, in this concentration range).

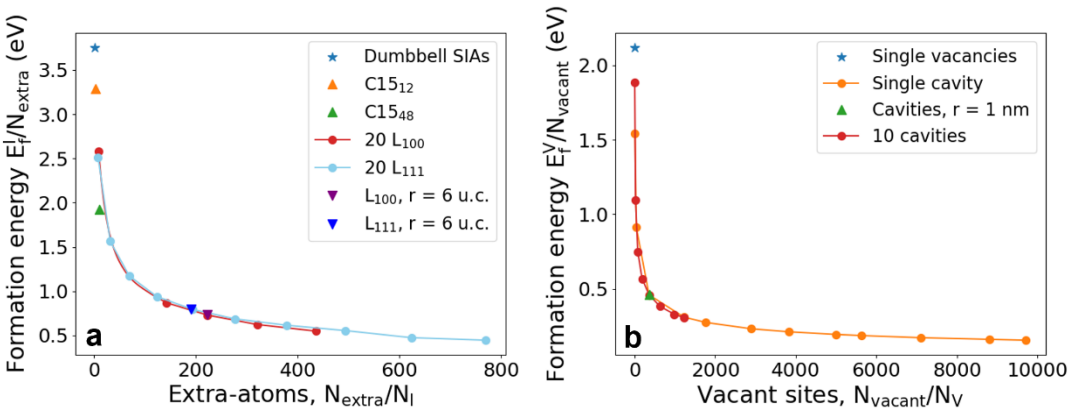


Fig. A2. Defect formation energies, E_f. a) Energy of interstitial-type defects per extra-atom (E_f^I/N_{extra}) as a function of the defect size (N_{extra}/N_I). b) Energy of vacancy-type defects per vacant site (E_f^V/N_{vacant}) as a function of defect size (N_{extra}/N_V). Defect types are explicitly mentioned in the figure captions, with L_{100} and L_{111} referring to <100> and ½<111> dislocation loops, respectively. r is the defect radius. Cells with dislocation loops of fixed radius (upside down triangle dots) contain 4 loops.